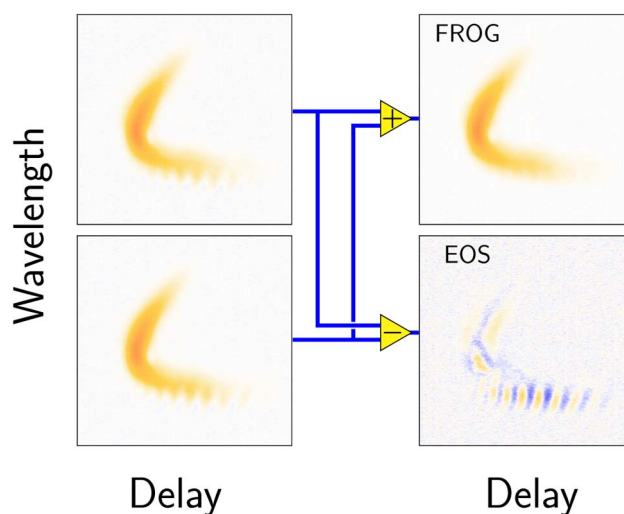


Real-Time Waveform Characterization by Using Frequency-Resolved Optical Gating Capable of Carrier-Envelope Phase Determination

Volume 6, Number 3, June 2014

Hideto Shirai
Yutaka Nomura
Takao Fuji



DOI: 10.1109/JPHOT.2014.2319091
1943-0655 © 2014 IEEE

Real-Time Waveform Characterization by Using Frequency-Resolved Optical Gating Capable of Carrier-Envelope Phase Determination

Hideto Shirai, Yutaka Nomura, and Takao Fuji

Institute for Molecular Science, Okazaki 444-8585, Japan

DOI: 10.1109/JPHOT.2014.2319091

1943-0655 © 2014 IEEE. Translations and content mining are permitted for academic research only. Personal use is also permitted, but republication/redistribution requires IEEE permission. See http://www.ieee.org/publications_standards/publications/rights/index.html for more information.

Manuscript received March 6, 2014; revised April 16, 2014; accepted April 17, 2014. Date of publication April 22, 2014; date of current version May 9, 2014. This work was supported in part by MEXT/JSPS KAKENHI under Grant 24360030, by SENTAN JST (Japan Science and Technology Agency), by the RIKEN-IMS Joint Programme on “Extreme Photonics,” and by the Consortium for Photon Science and Technology. Corresponding author: T. Fuji (e-mail: fuji@ims.ac.jp).

Abstract: We present real-time waveform characterization of ultrashort pulses by the use of a pulse-front tilt in frequency-resolved optical gating capable of carrier-envelope phase determination. Simultaneous measurement of cross-correlation frequency-resolved optical gating and electro-optic sampling signals has been realized without scanning any delays. Complete waveform characterization of single-cycle infrared pulses in real time has been demonstrated. The method has been also applied for characterization of more complex pulses, namely, a strongly chirped pulse after passing through a solid crystal or a distorted pulse due to the absorption of ambient air.

Index Terms: Ultrashort pulse measurements, four wave mixing.

1. Introduction

Recently developed optical waveform synthesis technology allows us to generate isolated single-cycle pulses [1]–[3]. Such a light source becomes important for latest high-field physics, for example, investigations of high-harmonic generation and strong-field ionization [4]. However, proper characterization of a single-cycle pulse is always challenging. The spectrum of a single-cycle pulse spans more than one octave and its carrier-envelope phase (CEP) strongly affects the shape of its electric-field. In particular, single-shot or real-time characterization of a single-cycle pulse is often essential for high-field physics.

It is possible to characterize a single-cycle pulse without its CEP information by using the already existing schemes like frequency-resolved optical gating (FROG) [5], [6] or spectral shearing interferometry for electric-field reconstruction (SPIDER) [7], [8]. Extremely thin second-order nonlinear crystals were used to achieve large phase matching bandwidths [1], [2]. However, the CEP cannot be determined by the use of FROG or SPIDER alone.

A straightforward technique to characterize single-cycle pulses is the use of attosecond pulses. It becomes possible to obtain the electric field oscillation of a single-cycle pulse by measuring a cross-correlation signal between extreme-ultraviolet (XUV) attosecond pulse and the single-cycle pulse. One of the most famous such methods is attosecond streaking [3], [9], and very recently it has been demonstrated that the cross-correlation between an XUV attosecond pulse and a visible

electric field can be obtained with the measurement of angular distribution of the XUV attosecond pulse [10]. However, these techniques are not very common technology yet. A high intensity laser and high vacuum systems are necessary. In addition, the field measurement scheme mentioned above does not have capability of single-shot detection.

Electro-optic sampling (EOS) [11] can be considered as a technology to characterize a single-cycle pulse including its CEP information. It is a very common technique to measure the field evolution of terahertz pulses. However, the method requires a reference pulse shorter than the period of the electric-field to be characterized as is the same as the attosecond streaking. The scheme has been used in a rather long wavelength region, specifically, from terahertz to infrared region [12]–[14].

Recently, we have proposed a new pulse characterization concept, FROG capable of CEP determination (FROG-CEP) [15]. The concept is based on a combination of FROG and EOS, which enables us to determine not only the intensity and (relative) phase profile of a single-cycle pulse but also CEP at the same time. We have demonstrated the pulse characterization of a single-cycle infrared pulse including its CEP information by using the new concept.

In this paper, we summarize the detail of the *real-time* waveform measurement of single-cycle infrared pulses using FROG-CEP. Here, a *real-time* measurement means a measurement without any moving parts. There are two important aspects in the waveform measurement technology to monitor the waveform of a single-cycle pulse in real-time. One is the use of a gas as a nonlinear medium with low dispersion. The other is the use of pulse-front tilt to map the delay of the FROG measurement onto transverse position on the plane where the nonlinear interaction occurs. We have succeeded in incorporating these two aspects in FROG-CEP and demonstrating waveform measurements of single-cycle infrared pulses without scanning any delays, which fact implicates single-shot capability of FROG-CEP. The CEP control of the single-cycle pulses was clearly observed with the method. Furthermore, we have applied the method to characterize more complex pulses, one is a significantly chirped pulse after passing through a 8-mm thick potassium bromide (KBr) crystal, and the other is a distorted pulse due to the absorption of ambient air. While we have published the real-time FROG-CEP as a part of the previous manuscript [15], the aim of the present paper is to provide more detail of the experimental conditions and the precise comparison between the scanning and real-time modes. In addition, we show that the scheme is capable to characterize rather complex pulses.

The paper is structured as follows. In Section 2, we briefly discuss how we should use gas media for both FROG and EOS. In Section 3, we explain the detail of the experimental setup for the real-time FROG-CEP with the theoretical description of the measurement scheme. In Section 4, we show the results of single-cycle infrared pulse characterization with the explanation of the retrieval process. In Section 5, we show the results of characterization for more complex pulses with the same method. In the last section, we provide some general conclusions and future prospects of the method.

2. Gas Media for Pulse Characterization

2.1. Gas Media for FROG

The use of a gas as a nonlinear medium instead of a solid for FROG would be very helpful for obtaining the spectral phase for an ultrabroadband spectral range. Although one has to suffer from the low efficiency of the nonlinear interaction due to the low nonlinear refractive index and the necessity of the nonlinear effect higher than third order due to the centrosymmetry [16], very large acceptance bandwidth is guaranteed due to the much weaker dispersion of gas media.

However, it has to be noted that some nonlinear mixing processes in gases have some finite response time even when the medium is transparent in the wavelength region of the input pulses. Transient-grating FROG by the use of air as a nonlinear medium was demonstrated in 1997 [17]. In that paper, it is mentioned that the nonlinear response function of air for the transient-grating is dominated by non-resonant Raman process, such as molecular rotation and/or vibration. The

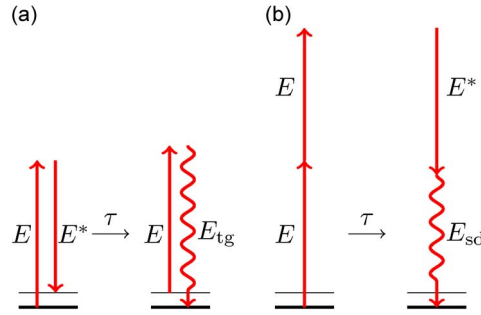


Fig. 1. Energy diagrams for non-resonant (a) transient-grating and (b) self-diffraction processes for FROG. E is the input electric field. E_{tg} and E_{sd} are the electric fields of the transient-grating and the self-diffraction, respectively. τ is the delay between the two replica of the input electric field.

effective response time is estimated as ~ 130 fs at room temperature even though the medium does not have any absorption in the wavelength range of the input pulse. To characterize the pulse whose duration is shorter than 100 fs pulse, at least the response function of the molecular rotation or vibration should be known [6], [18], or a noble gas, which does not have any rotation or vibration levels, should be used as the nonlinear medium [19].

On the other hand, it is not the case for self-diffraction FROG although both self-diffraction and transient-grating are four-wave mixing processes. The response time for the self-diffraction is only limited by the dephasing time of the nonlinear medium. Therefore, as long as the medium does not have any resonance for one- or two-photon absorption, the response time can be assumed as instantaneous for the self-diffraction process. The difference can be seen in the following equations:

$$E_{tg}(t, \tau) \propto |E(t - \tau)|^2 E(t) \quad (1)$$

$$E_{sd}(t, \tau) \propto E^2(t - \tau) E^*(t) \quad (2)$$

where $E(t)$, $E_{tg}(t, \tau)$, and $E_{sd}(t, \tau)$ are the electric fields of the input pulse, the transient grating signal, and the self-diffraction signal, respectively. τ is the delay between the two replica of the input pulses. The energy diagram in Fig. 1 also shows clear difference between the two processes. If there is a rotational or vibrational level and the energy gap between the ground state and the excited state is smaller than the bandwidth of the input pulse, the response function of the diffraction by the transient grating depends on the coherence time of the excited state. On the other hand, it is clear from the energy diagram that the response time of the self-diffraction is not related to the excited state.

Cross-correlation FROG (XFROG [20]) with four-wave difference frequency generation in nitrogen has been demonstrated to characterize single-cycle 7-fs infrared pulses [21], [22]. The four-wave difference frequency (FWDF) signal can be written as

$$E_{fwm}(t, \tau) \propto E_{ref}^2(t - \tau) E_{test}^*(t) \quad (3)$$

where the FWDF, reference, and test (infrared) electric fields are $E_{fwm}(t, \tau)$, $E_{ref}(t - \tau)$, and $E_{test}(t)$, respectively. τ is the delay between the reference and test electric fields. The response of the nonlinear process is not dominated by non-resonant Raman processes either. It is easy to understand by considering that the process is essentially the same as self-diffraction when the same electric field is substituted for the input fields, $E_{ref}(t - \tau)$ and $E_{test}(t)$, in eq. (3). In addition, we have confirmed that no difference of the FROG trace was observed at the experiment when the gas for the nonlinear interaction was changed from argon to nitrogen.

2.2. Gas Media for EOS

EOS with a gas medium is already known as air-biased coherent detection (ABCD) for terahertz waveform measurement [23]. The basic principle of ABCD is the measurement of interference

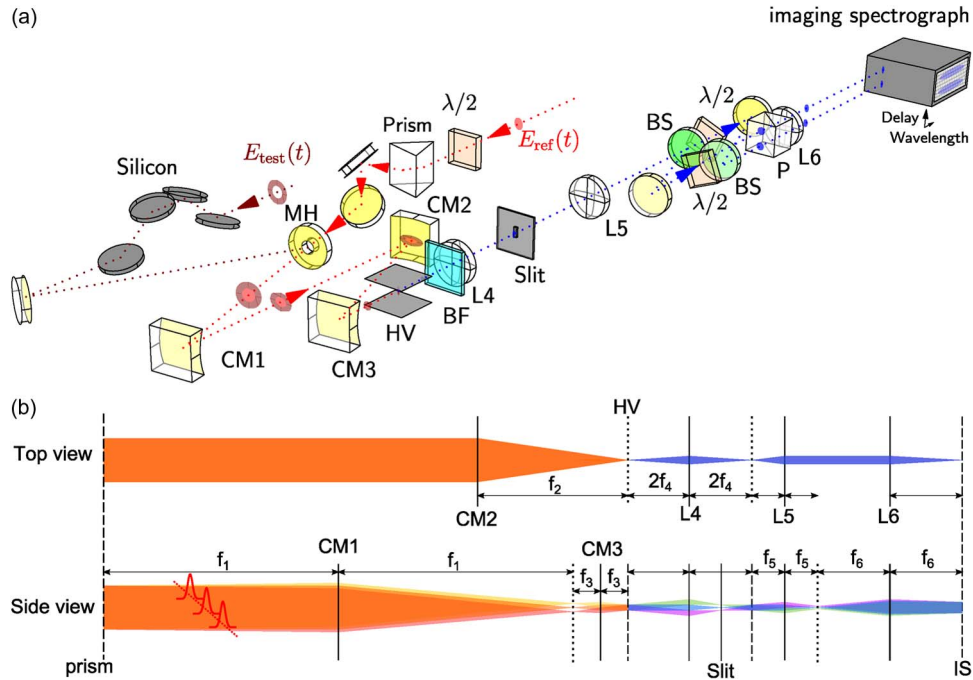


Fig. 2. (a) Schematic of the real-time waveform measurement. Prism: CaF_2 Brewster prism, MH: mirror with a hole, CM1–3: concave cylindrical mirrors ($f_1 = 1000$ mm, $f_2 = 190.7$ mm, and $f_3 = 51.9$ mm, respectively), HV: high voltage (4 kV), BF: blue filter (FGB37, Thorlabs), L4–6: achromatic lens ($f_4 = 75$ mm, $f_5 = 75$ mm, $f_6 = 500$ mm, respectively), BS: 50% beam splitter for 400–500 nm, $\lambda/2$: half-wave plate for 400–700 nm (10RP52-1, Newport), P: calcite polarizer. (b) Conceptual diagram of the imaging system. The red dashed line shows pulse front of the reference pulse tilted with the prism. In the vertical direction (see Side view), the back surface of the prism is imaged on the plane where the nonlinear interaction occurs (HV) and the entrance slit of the imaging spectrograph (IS). Black dashed lines: image planes; black solid lines: positions of focusing optics; black dotted lines: Fourier planes.

between terahertz-field-induced second harmonic and bias-field-induced second harmonic through third order nonlinear processes. These signals can be written as

$$E_{\text{sh}}^{\text{THz}}(t, \tau) \propto E_{\text{ref}}^2(t - \tau) E_{\text{thz}}^*(t) \quad (4)$$

$$E_{\text{sh}}^{\text{DC}}(t, \tau) \propto E_{\text{ref}}^2(t - \tau) E_{\text{bias}} \quad (5)$$

where $E_{\text{sh}}^{\text{THz}}$, $E_{\text{sh}}^{\text{DC}}$, E_{thz} , and E_{bias} are terahertz-field-induced second harmonic, bias-field-induced second harmonic, terahertz, and DC-bias fields, respectively. These processes are basically the same as four-wave difference frequency generation, therefore, the response time of the nonlinear medium can be assumed as instantaneous as long as the medium is transparent as is discussed in the previous subsection.

3. Experimental Setup

The challenge of the real-time FROG-CEP is simultaneous real-time measurement of FROG and EOS signals using a gas as the nonlinear medium. Either real-time FROG with gas medium or real-time ABCD has not been reported yet although single-shot version of FROG and EOS with solid media have been demonstrated [5], [24]–[27].

Experimental demonstration of the real-time observation of single-cycle light field was realized with the system shown in Fig. 2(a). The system was basically constructed for realization of simultaneous measurement of XFROG and EOS signals. The light source was based on a Ti:sapphire multi-pass amplifier system (800 nm, 30 fs, 0.85 mJ at 1 kHz, Femtopower compactPro, FEMTOLASERS). We generated CEP-stable infrared single-cycle pulses ($E_{\text{test}}(t), \omega_0$) by using four-wave mixing ($\omega_1 + \omega_1 - \omega_2 \rightarrow \omega_0$) of the fundamental (800 nm, ω_1) and SH (400 nm, ω_2) of

Ti:sapphire amplifier output through filamentation in nitrogen [22]. The stability of the CEP was estimated as $\sim 0.1(0.03\pi)$ rad rms for 2 seconds. The generated infrared pulse was reflected by four Si plates at the Brewster angle (75°) to purify the polarization of the infrared pulse, and the whole path for the infrared pulse was purged with nitrogen.

A small portion of the fundamental beam was used as a reference pulse. The reference pulse ($E_{\text{ref}}(t - \tau)$) with the beam size of 8 mm ($1/e^2$ width) was sent through a calcium fluoride (CaF_2) Brewster prism so that the beam had a pulse-front tilt. The detectable temporal range obtained with the pulse front tilt was about 450 fs. Not only the delay but also the dispersion experienced at each transverse position is different. We minimized the amount of the chirp of the reference pulse at the central part of the transverse position. The residual group delay dispersion at each edge of the transverse position is estimated as $\pm 223 \text{ fs}^2$, which introduces temporal broadening from 30 fs to 36 fs at each position. This pulse length inhomogeneity does not affect the FROG result too much. In addition, it would be even possible to include the inhomogeneity of the reference pulse duration in the retrieval algorithm. The beam which passed through the prism was rotated by 90° with a periscope to have the pulse front tilt in the vertical direction.

The reference pulse (ω_1) was combined with the infrared pulse (ω_0) through a mirror with a hole. To avoid undesirable spatio-temporal distortions due to the prism, the back surface of the prism was imaged by using a few cylindrical mirrors onto the plane where the nonlinear mixing occurred. The detail of the imaging geometry is shown in Fig. 2(b). The precise imaging was confirmed by putting a mask very close to the prism and observing the image of the beam with a CCD camera. The beam was elliptical at the nonlinear interaction plane (HV in Fig. 2), the vertical and horizontal $1/e^2$ width being $400 \mu\text{m}$ and $50 \mu\text{m}$, respectively. The size of the beam was minimum and the intensity of the beam was maximum at the plane. The FWDF ($\omega_1 + \omega_1 - \omega_0 \rightarrow \omega_2$) signal, $E_{\text{fwm}}(t, \tau) \propto -i\chi_{yyxx} E_{\text{ref}}^2(t - \tau) E_{\text{test}}^*(t)$, was generated at the plane, HV, where χ_{yyxx} is the third-order nonlinear susceptibility represented with the tensors with the four subscripts corresponding to polarizations of the FWDF, infrared, the fundamental and the fundamental beams, respectively. The polarizations of the reference pulse and the infrared pulse were perpendicular to each other, and the polarization of the generated FWDF signal was parallel to the infrared pulse and perpendicular to the reference pulse. We did not observe any four-wave sum frequency signal ($\omega_1 + \omega_1 + \omega_0 \rightarrow \omega_2$), $E_{\text{fwm}}(t, \tau) \propto -i\chi_{yyxx} E_{\text{ref}}^2(t - \tau) E_{\text{test}}(t)$, because the phase mismatch caused by the Gouy phase shift was too large [28].

To detect EOS signal, we produce the SH of the reference pulse, $E_{\text{shg}}(t - \tau) \propto -i\chi_{xxxx} E_{\text{ref}}^2(t - \tau) E_{\text{bias}}$, as a local oscillator field at the position HV by applying a DC bias field (E_{bias}) to Rogowski-type electrodes [29] with a distance of 3 mm by two high voltage amplifiers (HEOPS-5B6, Matsusada) with an amplitude of $\pm 4 \text{ kV}$, which corresponds to 27 kV/cm field strength. The direction of the electric field was parallel to the polarization of the reference pulse, and the FWDF signal and the bias induced SH have polarizations perpendicular to each other. The system and the principle to detect the EOS signal is basically the same as balanced terahertz wave ABCD [30].

Fig. 3 shows the images of the SH of the reference pulses (without FWDF signal) recorded with the imaging spectrograph. Some distortion due to the self-focusing of the reference pulse in the image at the nonlinear interaction plane was observed when the pulse energy of the reference pulse was larger than $150 \mu\text{J}$. Therefore, we have to work with the reference pulse less than $150 \mu\text{J}$ pulse energy in this situation.

In general, a Wollaston prism is used in the ellipsometry technique at EOS [30]. However, the chromatic dispersion of the Wollaston prism cannot be ignored in this study since the spectrum of the FWDF signal spread from 400 nm to 500 nm. We had to use a following rather complex optical system to avoid such chromatic dispersion in the ellipsometry technique. The FWDF signal was split by a 1 : 1 broadband beam splitter (400–500 nm) with approximately normal incidence to have the same separation ratio for any polarizations. The polarizations of the two beams were rotated by 45° and -45° , respectively by using achromatic zero-order quartz- MgF_2 half wave plates (10RP52-1, Newport) so that the two beams were cross-polarized to each other. The two beams were horizontally aligned but vertically displaced on the other beam splitter. The beams passed

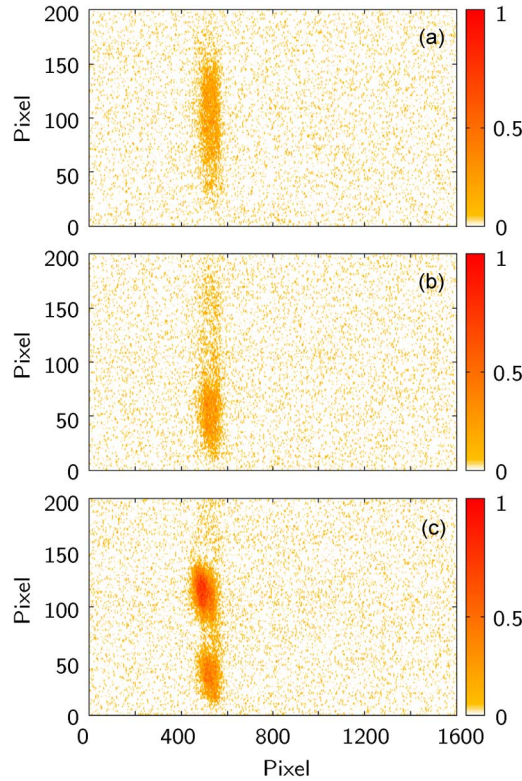


Fig. 3. Images of the SH of the reference pulse recorded with the imaging spectrograph. The horizontal axis corresponds to wavelength, and the vertical axis corresponds to transverse position of the SH beam. The energies of the reference pulse are (a) 150 μJ , (b) 200 μJ , and (c) 300 μJ , respectively.

through a calcite polarizer and only the horizontally polarized components transmitted. The averaged intensity of one of the beams, $I(\tau)$, can be explained as

$$I(\tau) = \langle |E(t, \tau)|^2 \rangle = \langle |(E_{\text{shg}}(t - \tau) \sin 2\theta + E_{\text{fwm}}(t, \tau) \cos 2\theta)|^2 \rangle \quad (6)$$

$$= \langle |E_{\text{shg}}(t - \tau) \sin 2\theta|^2 \rangle + \langle |E_{\text{fwm}}(t, \tau) \cos 2\theta|^2 \rangle + \langle 2\Re\{E_{\text{shg}}(t - \tau)E_{\text{fwm}}^*(t, \tau) \cos 2\theta \sin 2\theta\} \rangle \quad (7)$$

where $E(t, \tau)$ is the electric field of the beam, and θ is the angle of the half wave plate.

The transmitted beams were focused into an imaging spectrograph with an EMCCD camera (SP-2358 with ProEM + 1600, Princeton Instruments). We recorded two vertically displaced traces simultaneously. The vertical axis and the horizontal axis of each trace represent the delay and the wavelength, respectively. The two traces ($I_1(\omega, \tau)$, $I_2(\omega, \tau)$) are calculated from the Fourier-transform of $E(t, \tau)$ after substituting $\theta = \pi/8$ and $\theta = -\pi/8$, respectively

$$I_1(\omega, \tau) = \left| \left(\frac{1}{\sqrt{2}} \tilde{E}_{\text{shg}}(\omega) \exp(-i\omega\tau) + \frac{1}{\sqrt{2}} \tilde{E}_{\text{fwm}}(\omega, \tau) \right) \right|^2$$

$$= \frac{1}{2} |\tilde{E}_{\text{shg}}(\omega)|^2 + \frac{1}{2} |\tilde{E}_{\text{fwm}}(\omega, \tau)|^2 + \Re\{ \tilde{E}_{\text{shg}}(\omega) \tilde{E}_{\text{fwm}}^*(\omega, \tau) \exp(-i\omega\tau) \} \quad (8)$$

$$I_2(\omega, \tau) = \left| \left(-\frac{1}{\sqrt{2}} \tilde{E}_{\text{shg}}(\omega) \exp(-i\omega\tau) + \frac{1}{\sqrt{2}} \tilde{E}_{\text{fwm}}(\omega, \tau) \right) \right|^2$$

$$= \frac{1}{2} |\tilde{E}_{\text{shg}}(\omega)|^2 + \frac{1}{2} |\tilde{E}_{\text{fwm}}(\omega, \tau)|^2 - \Re\{ \tilde{E}_{\text{shg}}(\omega) \tilde{E}_{\text{fwm}}^*(\omega, \tau) \exp(-i\omega\tau) \} \quad (9)$$

where $\tilde{E}_x(\omega)$ denotes Fourier transform of $E_x(t)$ for each subscript.

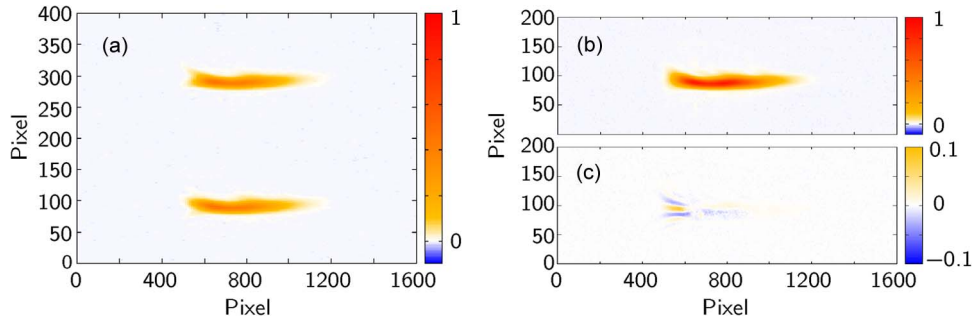


Fig. 4. (a) A typical image recorded with the spectrograph. The sum (b) and difference (c) of the two traces in (a) are also shown.

Fig. 4(a) shows a typical image recorded with the spectrograph. The spectrum contributed from the delay independent first term, $(1/2)|\tilde{E}_{\text{shg}}(\omega)|^2$, is subtracted. The size of the CCD was 1600×400 pixels. The exposure time of the camera was 2 seconds, corresponding to averaging 2000 shots, to achieve a reasonable signal-to-noise ratio in the current condition. The delay time axis was calibrated by measuring the relation between the displacement of the delay stage and a shift of the traces. The calibration value for the time axis was 1.86 fs/pixel, and the time window was 372 fs.

The sum of the two traces, $I_{\text{SUM}}(\omega, \tau)$, reflects the XFROG signal, and the difference between the two spectra, $I_{\text{DIF}}(\omega, \tau)$, reflects the EOS signal. These signals can be written as

$$I_{\text{SUM}}(\omega, \tau) \propto \left| \int d\omega' \chi_{yyxx}^{(3)} \exp(-i\omega'\tau) \tilde{E}_{\text{ref2}}(\omega') \tilde{E}_{\text{test}}^*(-\omega + \omega') \right|^2 \quad (10)$$

$$I_{\text{DIF}}(\omega, \tau) \propto 2\Re \left\{ \int d\omega' \chi_{xxxx}^{(3)} \chi_{yyxx}^{(3)} E_{\text{bias}} \exp(i\omega'\tau) \tilde{E}_{\text{ref2}}(\omega) \tilde{E}_{\text{ref2}}^*(\omega + \omega') \tilde{E}_{\text{test}}(\omega') \right\} \quad (11)$$

where $\tilde{E}_{\text{ref2}}(\omega)$ is the Fourier transform of $E_{\text{ref}}^2(t)$. When $I_{\text{DIF}}(\tau, \omega)$ is integrated along ω , we obtain

$$\begin{aligned} I_{\text{DIF}}(\tau) &\equiv \int d\omega I_{\text{DIF}}(\omega, \tau) \\ &\propto 2C \cdot \Re \left\{ \int d\omega' \exp(i\omega'\tau) \left[\int d\omega \tilde{E}_{\text{ref2}}(\omega) \tilde{E}_{\text{ref2}}^*(\omega + \omega') \right] \tilde{E}_{\text{test}}(\omega') \right\} \\ &= 2C \cdot \Re \left\{ \int d\tau' E_{\text{test}}(\tau') |E_{\text{ref}}^2(\tau' - \tau)|^2 \right\} \end{aligned} \quad (12)$$

where $C = \chi_{xxxx}^{(3)} \chi_{yyxx}^{(3)} E_{\text{bias}}$. This is the full information of the test pulse field ($\Re\{E_{\text{test}}(t)\}$) convoluted with $|E_{\text{ref}}(t)|^2$.

Fig. 4(b) and (c) show the sum and difference of the two images shown in Fig. 4(a), respectively. The sum corresponds to an XFROG trace, and the difference corresponds to a spectrally resolved EOS signal.

4. Electric-Field Retrieval

The process of the field retrieval is as follows. (i) The EOS signal, $I_{\text{DIF}}(\tau)$, is obtained by integrating the spectrally resolved EOS signal, $I_{\text{DIF}}(\omega, \tau)$, along the wavelength axis. The signal is shown as the blue solid curve in Fig. 5(a). (ii) The amplitude and phase of the EOS signal in frequency-domain are obtained through Fourier transform of $I_{\text{DIF}}(\tau)$. The signals are shown as the blue shaded curve and open squares in Fig. 5(b), respectively. (iii) The intensity and phase of the test pulse in frequency domain are obtained from the sum, $I_{\text{SUM}}(\omega, \tau)$, through an XFROG retrieval algorithm. The red shaded curve and closed circles in Fig. 5(b) show spectral distribution and phase, respectively. (iv) The spectral phase obtained with the XFROG is corrected by shifting it so that the spectral phases from XFROG and EOS match in the overlapped region. (v) The electric field of the

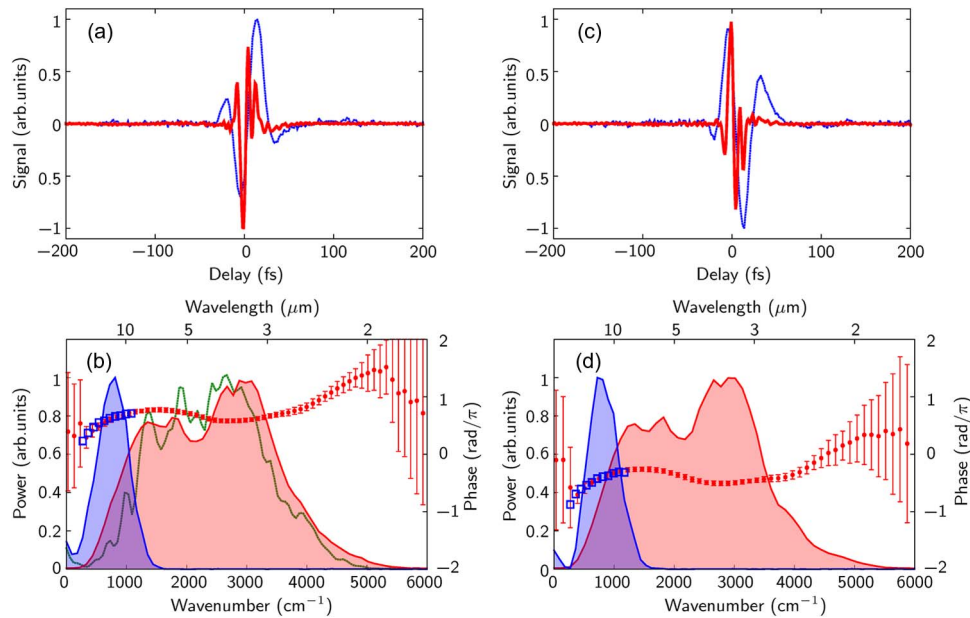


Fig. 5. Experimental results of the real-time measurement. (a) The blue solid curve was obtained by integrating the trace of Fig. 4(c) along the wavelength axis. The red solid curve shows electric fields reconstructed with the method described in text. (b) The red shaded curve is spectral distribution with XFROG. The red closed circles are the spectral phase after the offset correction. The offset of the spectral phase is corrected by using the phase information obtained with EOS. The green solid curve is the spectral distribution measured with Fourier transform spectrometer. The error bars of the phase are estimated with the bootstrap method. The blue shaded curve and open squares are the spectral distribution and spectral phase obtained from the Fourier transform of the EOS signal. (c) and (d) are results where the CEP of the pulse changed by π .

test pulse is obtained by Fourier transform of the XFROG result with the corrected phase. The retrieved electric field is shown as a red curve in Fig. 5(a).

The pulse duration of the test pulse is estimated to be 7.5 fs at 3.3 μm center wavelength, which corresponds to a sub-single-cycle pulse. The retrieved spectrum was nearly identical to the spectrum measured with a home-built Fourier-transform spectrometer (green curve in Fig. 5(b)).

The absolute phase at 3.3 μm was obtained as $-0.59\pi \pm 0.05\pi$. The accuracy of the spectral phases in the overlapped region obtained from the FROG and the EOS signals directly affect the accuracy of the waveform characterization. The phase obtained from the EOS signal can be defined very precisely since the oscillation period of the signal is much longer than the precision of the delay stage. The statistical error of the phase value from the EOS signal estimated through several measurements was $\sim 0.01\pi$. Determining the error of the spectral phase obtained from FROG is not so straightforward since the relationship between the measured data and retrieved values is complex in FROG. Here, we have obtained the error bars by using a bootstrap method [31], which is a well-established statistical resampling tool for determining uncertainty and has already been applied for estimation of error bars of phases obtained from FROG [32], [33]. We resample 128×128 points randomly with allowing to sample some points more than once and others not at all, and run XFROG retrieval for the new data set. We repeated the procedure 100 times and estimated the standard deviation of the phase. We assume that the phase of the reference pulse has no error. This assumption will only lead to overestimation of the error bars of the retrieved pulses because all the experimental errors will be attributed to the retrieved pulses. The estimated standard deviation of the phase in the overlapped region was 0.04π (see Fig. 5(b)). Therefore, the accuracy of the CEP turns out to be $\pm 0.05\pi$.

It can be seen that the spectra and electric fields obtained from the EOS signals are the results of filtering by the Fourier transform of $I_{\text{shg}}(t) \equiv |E_{\text{ref}}^2(t)|^2$. We can assume that the filtering function

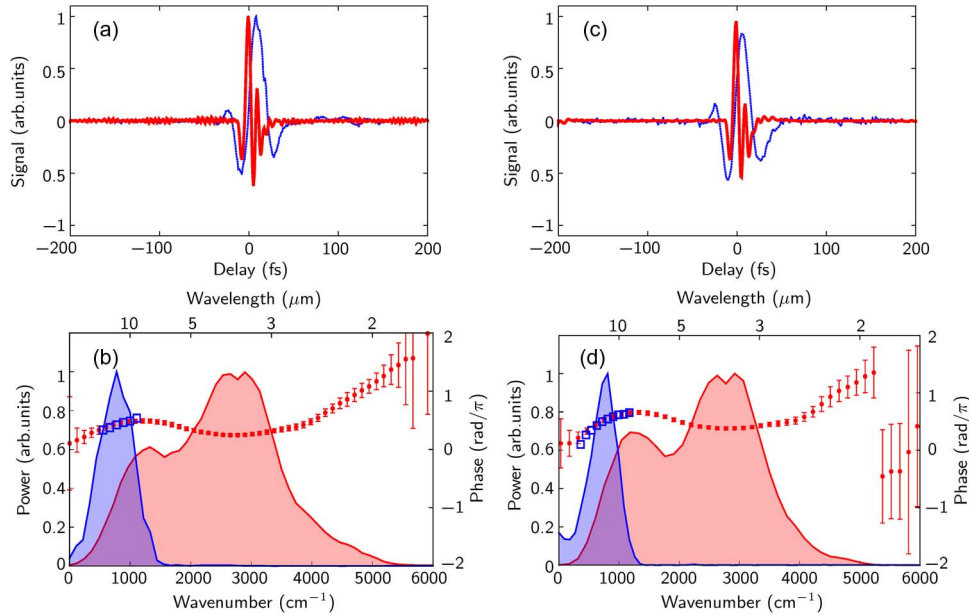


Fig. 6. Experimental results of the scanning and real-time operations. (a) and (b) are the results obtained by the scanning operation. (a) The blue solid curve was obtained by integrating the trace of along the frequency axis. The red solid curve shows the electric field reconstructed with the method described in text. (b) The red shaded curve is spectral distribution with XFROG. The red closed circles are the spectral phase after the offset correction. The offset of the spectral phase is corrected by using the phase information obtained with EOS. The blue shaded curve and open squares are the spectral distribution and spectral phase obtained from the Fourier transform of the EOS signal. (c) and (d) are the results obtained by the real-time operation for the same pulse.

does not affect the phase value. Since C in eq. (12) is real under our experimental condition, the only source which can make some additional phase shift is $\tilde{I}_{\text{shg}}(\omega) \equiv \int dt \exp(-j\omega t) I_{\text{shg}}(t)$. When the intensity of the reference pulse is symmetric in time, namely, $I_{\text{ref}}(-t) \sim I_{\text{ref}}(t)$, $\tilde{I}_{\text{shg}}(\omega)$ is real and thus there is no additional phase due to this function. Our reference pulse satisfies such condition, which was confirmed with the SHG-FROG measurement for the reference pulse.

Note that the slopes of the phases in the overlapped region coincide within the error bars, which means that the group delays from the two independent measurements are matched with each other. This fact strongly supports the consistency of the data sets.

We also demonstrate that the scheme indeed allows us to detect the change of CEP. It is known that the intensity of the infrared pulse generated by four-wave mixing changes with a period of ~ 200 nm by changing the delay between the fundamental and SH of the Ti:sapphire laser output pulses [22]. The situation is similar to terahertz generation with gas plasma [34], [35]. According to the reference, the CEP changes by π when the delay is changed by ~ 200 nm. We tuned the delay between the fundamental and SH by 200 nm and did the same measurement. Fig. 5(c) and (d) show the retrieved electric fields in time and frequency domain, respectively. As is expected, the intensity of the retrieved field does not change, whereas the CEP changes by π .

To check the reliability of the real-time operation, we also did scanning operation of the measurement and compared the results. The experimental setup is basically the same as the real-time operation shown in Fig. 2. We recorded the spectrum on one of the horizontal lines of the imaging spectrograph and scanned the delay time between the test and reference pulses using the optical delay stage (FS-1020SPX, Sigmatech) for the reference pulse. Fig. 6 shows experimental results of the scanning and real-time operations. The electric field of the infrared pulse was reconstructed in the same way as the real-time operation. The shapes of waveform and spectrum were almost identical to each other.

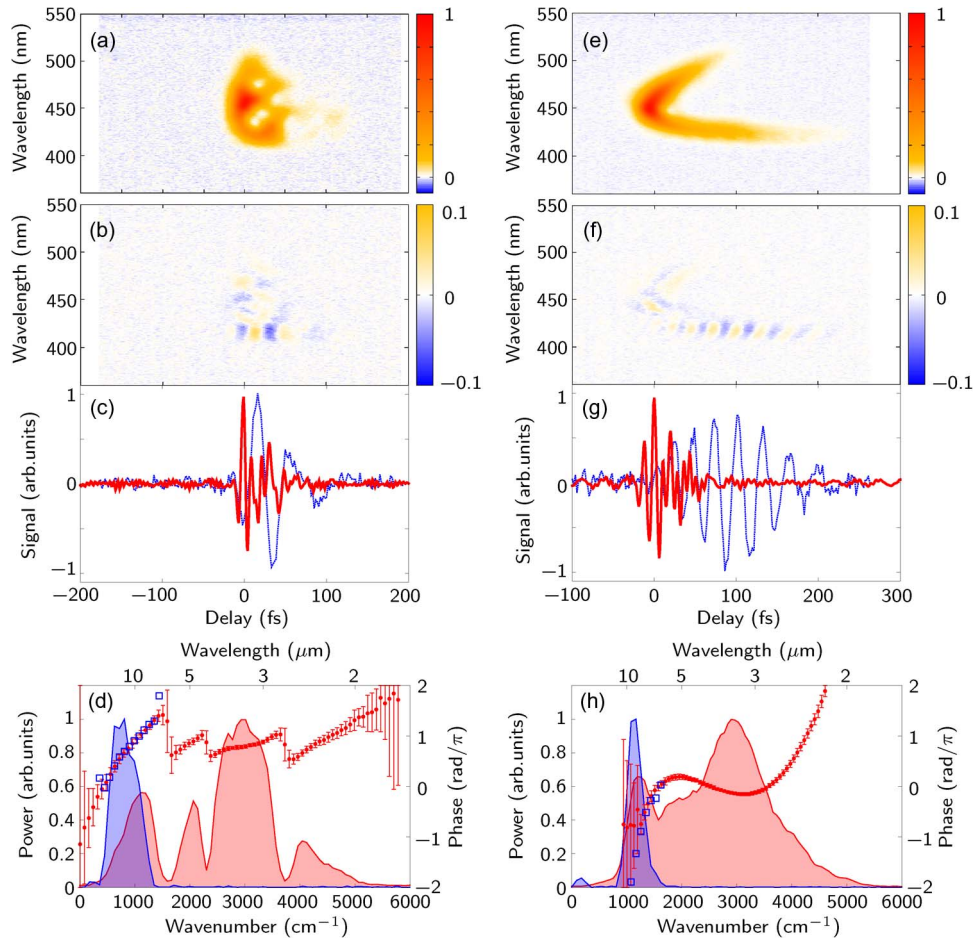


Fig. 7. Delay dependence of (a) sum and (b) difference of the two spectra of the infrared pulse passed through ambient air. (c) The blue solid curve was obtained by integrating the trace of (b) along the frequency axis. The solid curve shows electric fields reconstructed with the method described in text. (d) The red shaded curve is spectral distribution with XFROG. The red closed circles are the spectral phase after the offset correction. The offset of the spectral phase is corrected by using the phase information obtained with EOS. The blue shaded curve and open squares are the spectral distribution and phase obtained from Fourier transform of the EOS signal. (e)–(h) Results of the infrared pulse passed through the KBr crystal.

5. Measurement of Complex Waveforms

In order to investigate the application range of the method, we have applied it for the measurement of more complex pulses. Fig. 7(a)–(d) show the result of the infrared pulse after passing through ~ 1.5 m of the ambient air. The pulse is strongly distorted due to the absorption of air. The dips in the retrieved power spectrum correspond to the absorption lines of carbon dioxide (~ 2300 cm^{-1}) and water vapor (~ 1600 cm^{-1} and ~ 3700 cm^{-1}) although the time window of the measurement is too short to retrieve the real widths of the absorption lines. The phase shifts at the absorption lines are also clearly seen. Even for such a complex pulse, the slopes of the spectral phases retrieved from XFROG and EOS coincide very well in the overlapped region. The electric field of the infrared pulse was retrieved using the corrected phase value in the same way. Some oscillation due to the free induction decay of such the absorption lines can be clearly seen in time domain.

Fig. 7(e)–(h) show the characterization result of the infrared pulse after passing through a KBr crystal. The thickness of the KBr crystal was 8.0 mm and the path of the infrared pulse was purged with nitrogen. Complex phase distortion due to the dispersion of the crystal is even identified from

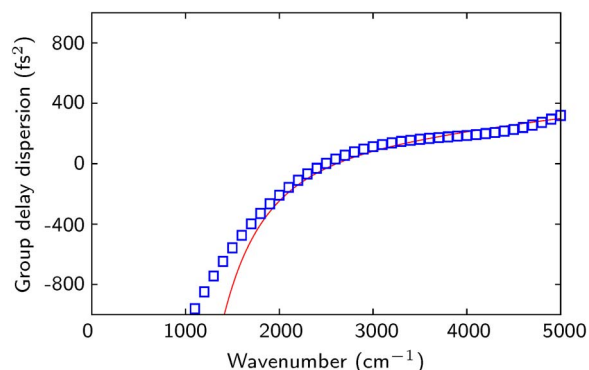


Fig. 8. Group delay dispersion of the KBr crystal. The blue open squares were obtained by the result of the FROG-CEP measurement shown in Fig. 7. The red solid line is the theoretical values calculated by the use of the Sellmeier equation for the crystal.

the XFROG trace (see Fig. 7(e)). In the low frequency region negative chirp is observed whereas positive chirp is observed in the high frequency region. The negative chirp is so strong that the low frequency component goes away from the time window of the measurement. This is the reason why the retrieved power spectrum lower than $\sim 1000\text{ cm}^{-1}$ is filtered out (see Fig. 7(h)).

The group delay dispersion (GDD) of the KBr crystal was estimated from the second order derivative of the spectral phase retrieved from the XFROG trace. Fig. 8 shows the comparison between the GDDs of the characterization result and the theoretical values calculated by the use of the Sellmeier equation for the crystal [36]. The values are well matched in the frequency region higher than 1500 cm^{-1} . The mismatch in the low frequency region is due to the short time window, which was too short to cover the whole length of the pulse. The time window can be enlarged by using a grating for the pulse front tilt instead of the prism [25]–[27].

6. Conclusion

In conclusion, we have summarized the real-time waveform characterization of single-cycle infrared pulses by the use of pulse front tilting. The result of the real-time measurement is nearly identical to that of the scanning measurement. We have also demonstrated that the method can be applied for more complex pulses which pass through absorptive or dispersive materials. The GDD of the dispersive material obtained with the technique has agreed well with the theoretical value.

The real-time FROG-CEP has capability for single-shot waveform characterization although averaging 2000 shots was necessary for reasonable signal-to-noise ratio in the current experimental condition. Since the required reference pulse energy for the measurement was $80\text{ }\mu\text{J}$, the necessary reference pulse energy for the single-shot measurement is estimated as 3.6 mJ , which is estimated by simply multiplying $80\text{ }\mu\text{J}$ by $\sqrt{2000}$. However, such a parameter strongly depends on the experimental conditions such as the wavelengths of the pulses or kinds of nonlinear interactions. In addition, the development of highly sensitive and fast scientific CMOS cameras would be helpful to realize the single-shot detection.

One of the most interesting applications of the scheme is waveform characterization of the pulses delivered from a free electron laser. Currently, our method would be one of the best candidates to characterize the waveform of the optical pulses, whose spectrum and CEP changes shot-by-shot.

References

- [1] G. Krauss *et al.*, “Synthesis of a single cycle of light with compact erbium-doped fibre technology,” *Nat. Photon.*, vol. 4, no. 1, pp. 33–36, Jan. 10, 2010.
- [2] S.-W. Huang *et al.*, “High-energy pulse synthesis with sub-cycle waveform control for strong-field physics,” *Nat. Photon.*, vol. 5, no. 8, pp. 475–479, Aug. 2011.

- [3] A. Wirth *et al.*, "Synthesized light transients," *Science*, vol. 334, no. 6053, pp. 195–200, Oct. 14, 2011.
- [4] F. Krausz and M. Ivanov, "Attosecond physics," *Rev. Mod. Phys.*, vol. 81, no. 1, pp. 163–234, Feb. 2009.
- [5] D. J. Kane and R. Trebino, "Single-shot measurement of the intensity and phase of an arbitrary ultrashort pulse by using frequency-resolved optical gating," *Opt. Lett.*, vol. 18, no. 10, pp. 823–825, May 1993.
- [6] R. Trebino, *Frequency-Resolved Optical Gating: The Measurement of Ultrashort Laser Pulses*. Norwell, MA, USA: Kluwer, 2000.
- [7] C. Iaconis and I. A. Walmsley, "Spectral phase interferometry for direct electric-field reconstruction of ultrashort optical pulses," *Opt. Lett.*, vol. 23, no. 10, pp. 792–794, May 1998.
- [8] C. Iaconis and I. A. Walmsley, "Self-referencing spectral interferometry for measuring ultrashort optical pulses," *IEEE J. Quantum Electron.*, vol. 35, no. 4, pp. 501–509, Apr. 1999.
- [9] E. Goulielmakis *et al.*, "Direct measurement of light waves," *Science*, vol. 305, no. 5688, pp. 1267–1269, Aug. 2004.
- [10] K. T. Kim *et al.*, "Petahertz optical oscilloscope," *Nat. Photon.*, vol. 7, no. 12, pp. 958–962, Dec. 2013.
- [11] Q. Wu and X.-C. Zhang, "Free-space electrooptic sampling of terahertz beams," *Appl. Phys. Lett.*, vol. 67, no. 24, pp. 3523–3525, Dec. 11, 1995.
- [12] R. Huber, A. Brodschelm, F. Tauser, and A. Leitenstorfer, "Generation and field-resolved detection of femtosecond electromagnetic pulses tunable up to 41 THz," *Appl. Phys. Lett.*, vol. 76, no. 22, pp. 3191–3193, May 29, 2000.
- [13] A. Sell, R. Scheu, A. Leitenstorfer, and R. Huber, "Field-resolved detection of phase-locked infrared transients from a compact Er: Fiber system tunable between 55 and 107 THz," *Appl. Phys. Lett.*, vol. 93, no. 25, pp. 251107-1–251107-3, Dec. 2008.
- [14] I. Katayama *et al.*, "Ultrabroadband terahertz generation using 4-N,N-dimethylamino-4'-N'-methyl-stilbazolium tosylate single crystals," *Appl. Phys. Lett.*, vol. 97, no. 2, pp. 021105-1–021105-3, Jul. 12, 2010.
- [15] Y. Nomura, H. Shirai, and T. Fujii, "Frequency-resolved optical gating capable of carrier-envelope phase determination," *Nat. Commun.*, vol. 4, p. 2820, Nov. 2013.
- [16] R. W. Boyd, *Nonlinear Optics*, 3rd ed. San Diego, CA, USA: Academic, 2008.
- [17] J. N. Sweetser, D. N. Fittinghoff, and R. Trebino, "Transient-grating frequency-resolved optical gating," *Opt. Lett.*, vol. 22, no. 8, pp. 519–521, Apr. 1997.
- [18] P. Lu *et al.*, "Cross-correlation frequency-resolved optical gating by molecular alignment for ultraviolet femtosecond pulse measurement," *Appl. Phys. Lett.*, vol. 97, no. 6, pp. 061101-1–061101-3, Aug. 2010.
- [19] J. Odhner and R. J. Levis, "Direct phase and amplitude characterization of femtosecond laser pulses undergoing filamentation in air," *Opt. Lett.*, vol. 37, no. 10, pp. 1775–1777, May 2012.
- [20] S. Linden, H. Giessen, and J. Kuhl, "XFROG—A new method for amplitude and phase characterization of weak ultrashort pulses," *Phys. Stat. Sol. (B)*, vol. 206, no. 1, pp. 119–124, Mar. 1998.
- [21] Y. Nomura *et al.*, "Phase-stable sub-cycle mid-infrared conical emission from filamentation in gases," *Opt. Exp.*, vol. 20, no. 22, pp. 24 741–24 747, Oct. 2012.
- [22] T. Fujii and Y. Nomura, "Generation of phase-stable sub-cycle mid-infrared pulses from filamentation in nitrogen," *Appl. Sci.*, vol. 3, no. 1, pp. 122–138, Feb. 2013.
- [23] N. Karpowicz *et al.*, "Coherent heterodyne time-domain spectrometry covering the entire 'terahertz gap'," *Appl. Phys. Lett.*, vol. 92, no. 1, pp. 011131-1–011131-3, Jan. 2008.
- [24] P. O'Shea, M. Kimmel, X. Gu, and R. Trebino, "Highly simplified device for ultrashort-pulse measurement," *Opt. Lett.*, vol. 26, no. 12, pp. 932–934, Jun. 2001.
- [25] J. Shan *et al.*, "Single-shot measurement of terahertz electromagnetic pulses by use of electro-optic sampling," *Opt. Lett.*, vol. 25, no. 6, pp. 426–428, Mar. 2000.
- [26] Y. Kawada, T. Yasuda, A. Nakanishi, K. Akiyama, and H. Takahashi, "Single-shot terahertz spectroscopy using pulse-front tilting of an ultra-short probe pulse," *Opt. Exp.*, vol. 19, no. 12, pp. 11 228–11 235, Jun. 2011.
- [27] Y. Minami, Y. Hayashi, J. Takeda, and I. Katayama, "Single-shot measurement of a terahertz electric-field waveform using a reflective echelon mirror," *Appl. Phys. Lett.*, vol. 103, no. 5, pp. 051103-1–051103-4, Jul. 2013.
- [28] G. C. Bjorklund, "Effects of focusing on 3rd-order nonlinear processes in isotropic media," *IEEE J. Quantum Electron.*, vol. QE-11, no. 6, pp. 287–296, Jun. 1975.
- [29] R. Kanya and Y. Ohshima, "Pendular-state spectroscopy of the S_1 – S_0 electronic transition of 9-cyanoanthracene," *J. Chem. Phys.*, vol. 121, no. 19, pp. 9489–9497, Nov. 2004.
- [30] X. Lu and X. C. Zhang, "Balanced terahertz wave air-biased-coherent-detection," *Appl. Phys. Lett.*, vol. 98, no. 15, pp. 151111-1–151111-3, Apr. 11, 2011.
- [31] W. H. Press, W. T. Vetterling, S. A. Teukolsky, and B. P. Flannery, *Numerical Recipes in C++: The Art of Scientific Computing*, 2nd ed. Cambridge, U.K.: Cambridge Univ. Press, 2002.
- [32] Z. Wang, E. Zeek, R. Trebino, and P. Kvam, "Beyond error bars: Understanding uncertainty in ultrashort-pulse frequency-resolved-optical-gating measurements in the presence of ambiguity," *Opt. Exp.*, vol. 11, no. 26, pp. 3518–3527, Dec. 2003.
- [33] Z. Wang, E. Zeek, R. Trebino, and P. Kvam, "Determining error bars in measurements of ultrashort laser pulses," *J. Opt. Soc. Amer. B, Opt. Phys.*, vol. 20, no. 11, pp. 2400–2405, Nov. 2003.
- [34] J. Dai and X. C. Zhang, "Terahertz wave generation from gas plasma using a phase compensator with attosecond phase-control accuracy," *Appl. Phys. Lett.*, vol. 94, no. 2, pp. 021117-1–021117-3, Jan. 12, 2009.
- [35] J. Dai, N. Karpowicz, and X. C. Zhang, "Coherent polarization control of terahertz waves generated from two-color laser-induced gas plasma," *Phys. Rev. Lett.*, vol. 103, no. 2, pp. 023001-1–023001-4, Jul. 2009.
- [36] M. Bass *et al.*, *Handbook of Optics, Third Edition Volume IV: Optical Properties of Materials, Nonlinear Optics, Quantum Optics (set), ser. Handbook of Optics*. New York, NY, USA: McGraw-Hill, 2009.